

# Tunable ultrastrong magnon–magnon coupling and spin Hall magnetoresistance in a van der Waals antiferromagnet

C. W. F. Freeman<sup>1,2,\*</sup>, Z. Xue<sup>1</sup>, H. Youel<sup>1</sup>, A.K. Budniak<sup>3,4</sup>, H. De Libero<sup>5</sup>, T. Thomson<sup>5</sup>,  
M. Bosman<sup>4,6</sup>, G. Eda<sup>3,7,8</sup>, H. Kurebayashi<sup>1,9,10</sup> & M. Cubukcu<sup>1,2,†</sup>

December 9, 2024

Antiferromagnetic (AFM) magnons and the manipulation of magnetisation via spin currents in van der Waals (vdW) materials offer substantial potential for applications in magnonics and spintronics. In this study, we demonstrate ultrastrong magnon-magnon coupling in the GHz regime within a vdW AFM, achieving a maximum normalised coupling strength of 0.89. Our investigation shows the tunability of coupling strength through temperature-dependent magnetic anisotropies. We compare coupling strength values derived from gap size with those calculated directly through the coupling parameter, showing that gap size as a measure of coupling strength is limited when intrinsic symmetry breaking induced magnon mode coupling is present. Additionally, analytical calculations show the possibility to reach the deep-strong coupling regime, with normalised coupling strengths greater than 1 by tuning the anisotropy values. Finally, we report on spin Hall magnetoresistance in a vdW AFM-based device and study the field and temperature dependence. These findings highlight the transformative potential of vdW AFMs in advancing the field of spin-based technologies.

**Keywords:** Spintronics, Magnonics, 2D Materials, Antiferromagnets, Spin Orbitronics

Within the expansive range of materials explored for spintronic applications, antiferromagnets (AFMs) have emerged as compelling candidates owing to their unique properties and potential to address challenges associated with traditional ferromagnetic (FM) devices [1, 2]. Characterized by the antiparallel alignment of neighboring magnetic moments, net zero magnetisation and atomistic exchange coupling strength, AFMs offer inherent advantages such as insensitivity to external magnetic fields and ultrafast spin dynamics [3]. However, the intricate nature of spin dynamics in AFMs presents both opportunities and challenges, underscoring the need for further investigation to fully harness their potential in spintronics.

Van der Waals (vdW) materials are layered materials that can be exfoliated down to monolayer structures relatively easily under controlled experimental conditions [4]. The recent discov-

ery of long-range magnetic order at the two-dimensional (2D) limit, which does not follow the Mermin-Wagner theorem [5] due to finite magnetic anisotropies, has stimulated an intense exploration of the growing variety of magnetic 2D materials [6, 7]. Similar to synthetic antiferromagnets (SyAF) [8], vdW AFM's such as  $\text{CrCl}_3$  [9] and  $\text{CrPS}_4$  [10] have a weak interlayer exchange coupling, which brings the typical terahertz (THz) dynamics of atomistic AFM's down to the gigahertz (GHz) regime. This characteristic makes them an ideal platform for studying a variety of spin dynamics phenomena using modern microwave techniques.

The interaction between magnons and other quasi-particles has garnered interest due to its fundamental importance in understanding complex quantum material interactions and its potential application in hybrid magnonics [11, 12]. Through leveraging the unique properties of magnons, these

<sup>1</sup> London Centre for Nanotechnology, University College London, London, WC1H 0AH, UK <sup>2</sup> National Physical Laboratory, Teddington, TW11 0LW, UK <sup>3</sup> Department of Physics, National University of Singapore, 117551, Singapore <sup>4</sup> Department of Materials Science & Engineering, National University of Singapore, 117581, Singapore <sup>5</sup> Department of Computer Science, University of Manchester, Manchester, M13 9PL, UK <sup>6</sup> Institute for Materials Research and Engineering, Agency for Science, Technology and Research (ASTAR), 138634, Singapore <sup>7</sup> Department of Chemistry, National University of Singapore, 117543, Singapore <sup>8</sup> Centre for Advanced 2D Materials, National University of Singapore, 117542, Singapore <sup>9</sup> Department of Electronic and Electrical Engineering, University College London, London, WC1E 7JE, UK <sup>10</sup> WPI-AIMR, Tohoku University, 2-1-1, Katahira, Sendai 980-8577, Japan \* uceecwf@ucl.ac.uk † m.cubukcu@ucl.ac.uk

systems have shown significant promise in quantum information processing, storage, and sensing [13, 14]. Due to the inherently weak dipolar interaction between magnons and photons, it is difficult to achieve ultrastrong magnon-photon coupling [15, 16]. The normalised coupling strength, defined as the ratio of the gap size to the bare excitation frequency, is typically used to quantify interaction regimes. When the normalised coupling strength increases above 0.1, the ultrastrong coupling regime is realized [17, 18, 19]. For light-matter systems in this regime, the rotating wave approximation no longer holds and the gap size is no longer a good representation of the coupling strength. To account for this more accurate models are adopted, such as the quantum Rabi model and Hopfield model [20]. In ultrastrong coupling systems, the interaction Hamiltonian consists of both the co-rotating and counter-rotating terms. This permits exotic physical phenomena, such as nontrivial ground states and superradiant phase transitions [21, 22, 23]. Recently the interaction between magnons themselves has emerged as a new avenue for investigating coupling phenomena [24, 9, 25, 26]. Unlike magnon-photon coupling, which are coupled through the relatively weak dipolar interaction, the intrinsically strong interaction between magnons results in an enhanced coupling strength, due to the spatial mode overlap through a shared host media [21].

Ultrastrong magnon-magnon coupling has been experimentally observed in compensated ferrimagnets, AFs, and SyAFs [27, 28, 24, 21]. Furthermore, vdW AFMs have been demonstrated as promising platforms for studying magnon-magnon coupling [9] where there is interest in studying magnon-magnon interaction in the ultrastrong coupling regime [29]. Li et al. [29] demonstrated that the symmetry breaking anisotropies arising from the crystal structure in CrPS<sub>4</sub> enable ultrastrong magnon-magnon coupling that can be controlled by varying the angle between the crystal axis and the applied magnetic field. Moreover, the deep-strong coupling regime has so far not been achieved in magnon-magnon interactions, with some recent studies in SyAF's reaching values near to this [21].

Quantifying the strength of magnon-magnon coupling remains a topic of considerable debate.

The gap size is commonly used as a measure of magnon-magnon coupling strength, serving as a tool to define ultrastrong interactions in magnon-magnon systems [27, 28, 24, 21, 26, 29]. It has been shown that when intrinsic symmetry breaking induces the coupling, that an indirect gap opening occurs between the resonance modes with further increased coupling strength [30]. Additionally, a dc-field independent coupling strength parameter has been proposed for defining this coupling, which can be derived from material parameters [30].

In addition to magnonics, the conversion of charge to spin currents is a crucial cornerstone of spintronics particularly for artificial intelligence and high-performance computing applications requiring high-speed on-chip memory [31, 32, 33]. Spin Hall Magnetoresistance (SMR) serves as a powerful tool for probing magnetisation states and spin transport phenomena in magnetic heterostructures. SMR in ferromagnetic/non-magnetic structures relies on the relative orientations of magnetisation and accumulated spins at the interface [34]. Although recent investigations into SMR in vdW materials have emerged, there are still few comprehensive studies [35, 36, 37]. The presence of electrical readout of magnetisation presents this system as a promising platform for future spin dynamics studies on thin flakes, for example using Spin-Torque Ferromagnetic Resonance (ST-FMR), which is highly desirable for exploration of the 2D nature of magnetism in vdW flakes [38].

In this work, we demonstrate ultrastrong magnon-magnon coupling in the vdW AFM material CrPS<sub>4</sub> in the GHz regime, achieving a normalised coupling strength of 0.89. We show how the orthorhombic magnetic anisotropy lowers the symmetry of the magnetic system, thereby inducing magnon-magnon coupling between the two resonance modes. Furthermore, we investigate the temperature dependence of this coupling and report the magnetic parameters as a function of temperature in the AFM regime. We demonstrate the tunability of coupling strength with temperature through controlling magnetic parameters, such as saturation magnetisation and the magnetic anisotropy. We compare coupling strength values derived from gap size with those calculated directly from magnetic properties. This comparison shows that gap size

as a measure of coupling strength is limited when intrinsic symmetry breaking drives magnon mode coupling. Additionally, we show that it is possible to tune this coupling strength the deep-strong regime with normalised coupling strengths greater than 1.

Moreover, we observe distinct spin transport effects on the magnetisation in a vdW AFM exfoliated flake at cryogenic temperatures using SMR. We fabricate a Pt/CrPS<sub>4</sub>/h-BN Hall bar device and measure the SMR as a function of magnetic field and temperature. This highlights the ability to electrically detect the magnetic state on exfoliated flakes within this system.

## Results and discussion

### Structure and magnetism in a vdW AFM

CrPS<sub>4</sub> is characterized by its semiconducting properties and an optically measured band gap of approximately 1.4 eV [39, 40]. The crystal structure exhibits non-centrosymmetry with monoclinic anisotropy, belonging to space group C<sub>2</sub>, with crystal axes of lengths  $a = 10.871 \text{ \AA}$ ,  $b = 7.254 \text{ \AA}$ ,  $c = 6.140 \text{ \AA}$ , and  $\beta = 91.88^\circ$  [41]. The crystal structure is illustrated in Fig. 1(a). In Fig. 1(b), we show X-ray diffraction of a single bulk CrPS<sub>4</sub> crystal. The position of 00x peaks is in agreement with A. Louisy et al. [40] confirming the successful growth of high quality CrPS<sub>4</sub>.

We initially focus on determining the magnetic properties of the bulk single crystal sample, we present the magnetometry results obtained from our crystal in two field orientations,  $H//c$  and  $H//ab$ , as functions of the applied magnetic field,  $H$ , and temperature,  $T$ . In Fig. 1(c), we depict the magnetisation,  $M$ , versus temperature under a small applied field (10 mT) perpendicular to the vdW plane. A sharp peak at 38 K followed by a steep decline is observed, indicative of the Néel transition temperature,  $T_N$ . This observed  $T_N$  of 38 K agrees well with literature-reported values [10]. Fig. 1(d) and 1(e) depict  $M$  versus  $H$  for the  $H//c$  and  $H//ab$  orientations, respectively, at temperatures ranging from 5 K to 50 K. For temperatures above 10 K, a

prominent non-saturating background is observed. From these we extract the saturation magnetisation as a function of temperature. In the  $H//c$  orientation, a characteristic spin-flop transition is evident due to the easy axis anisotropy of the material. The spin-flop transition is indicated by the plateau in the moment until reaching a critical field,  $H_{sf}$ . Beyond  $H_{sf}$ , a sharp increase in  $M$  is observed as the sublattices become canted towards the direction  $H$ . With increasing  $H$ , a linear rise in  $M$  is measured until saturation, as the angle between the sublattices and  $H$  decreases, ultimately saturating in the forced FM phase around 8 T at 5 K. The extracted values of  $M_s$  and  $H_{sf}$  are plotted as functions of temperature in Fig. 1(f), where both values decrease with increasing temperature.

### Spin dynamics in a vdW AFM

We now focus on ferromagnetic resonance (FMR) measurements conducted below the  $T_N$  for two orientations:  $H \perp c$  with  $\theta \approx 90^\circ$  and  $45^\circ$ , where  $\theta$  is the angle between the  $b$  axis and  $H$ . The crystal axis of the bulk crystal is determined visually, considering the straight edge of the crystal as the crystal growth aligns with the preferred  $b$  axis [10]. This method of determination differs from the preferential edges observed during exfoliation, which typically exhibit an angle of  $33.75^\circ$  away from the  $a$  axis [42, 39]. The experimental setup is depicted in Fig. 2(c).

### Tunable ultrastrong magnon–magnon coupling

Below, we present a detailed study of the temperature dependence of the resonances measured in the in-plane orientation with respect to the crystal axis,  $b$ , at angles  $\theta = 90^\circ$  and  $\theta \approx 45^\circ$ . Measurements in the out-of-plane orientation are included in the SI (Fig. S5).

To model the spin dynamics in an AFM system, we can employ a macrospin approach using the Landau-Lifshitz (LL) equation for two ferromagnetic sublattices. This approach results in coupled equations, allowing the calculation of frequency versus field spectra. Starting with Kittel's free en-

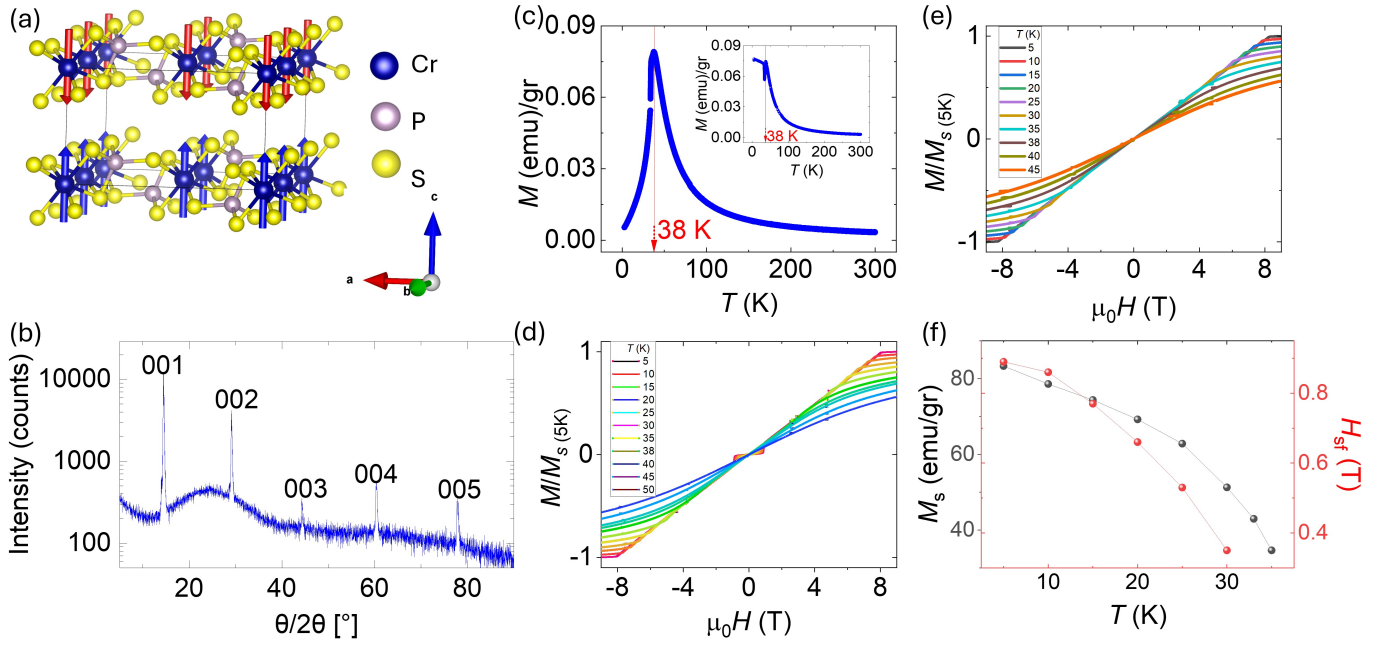


Figure 1: **Structure and magnetism in CrPS<sub>4</sub>.** a) Schematic illustration of crystal and magnetic structures of CrPS<sub>4</sub>. The blue and red arrows indicate the orientation of magnetic moments. b) X-ray diffraction of a single bulk CrPS<sub>4</sub> crystal. (c) Zero-field-cooled magnetisation ( $M$ ) of a CrPS<sub>4</sub> single crystal as a function of temperature ( $T$ ), with a 10 mT magnetic field applied parallel to the crystallographic  $c$ -axis. The red line indicates  $T_N$ . The inset illustrates the behavior under a magnetic field applied perpendicular to the  $c$ -axis. (d) Field-dependent normalised magnetisation ( $M / (M_{S(5K)})$ ) at various temperatures with the magnetic field ( $\mu_0 H$ ) oriented parallel to the  $c$ -axis. The inset provides a zoomed-in image around spin-flip transition ( $H_{sf}$ ). (e) Field-dependent normalised magnetisation at various temperatures with the field-oriented perpendicular to the  $c$ -axis. (f) Saturation magnetisation ( $M_s$ ) and spin-flop transition field ( $H_{sf}$ ) as a function of temperature ( $T$ ).

ergy equation for orthorhombic anisotropy and neglecting the terms dependent upon the relative positions of the sublattice moments [43]:

$$F_A = K_1/2(\alpha_1^2 + \beta_1^2) + K_2/2(\alpha_2^2 + \beta_2^2) \quad (1)$$

where  $F_A$  is the anisotropy component free energy,  $K_1$  and  $K_2$  are the anisotropy constants related to the  $a$  and  $b$  axis,  $\alpha_1$ ,  $\alpha_2$ ,  $\beta_1$  and  $\beta_2$  are the cosines of the unit magnetisation for the two sublattices. The LL equation can then be written as follows:

$$\begin{aligned} \frac{d\hat{m}_A}{dt} &= -\mu_0\gamma\hat{m}_A \times (\mathbf{H} - H_E\hat{m}_B - M_s(\hat{m}_A \cdot \hat{z})\hat{z} \\ &\quad - H_{A1}(\hat{m}_A \cdot \hat{x})\hat{x} - H_{A2}(\hat{m}_A \cdot \hat{y})\hat{y}), \\ \frac{d\hat{m}_B}{dt} &= -\mu_0\gamma\hat{m}_B \times (\mathbf{H} - H_E\hat{m}_A - M_s(\hat{m}_B \cdot \hat{z})\hat{z} \\ &\quad - H_{A1}(\hat{m}_B \cdot \hat{x})\hat{x} - H_{A2}(\hat{m}_B \cdot \hat{y})\hat{y}) \end{aligned} \quad (2)$$

where  $m_A$  and  $m_B$  are the moments of the two sublattices,  $\gamma$  is the gyromagnetic ratio and  $H_E$  denotes the interlayer exchange field. The anisotropy fields,  $H_{A1}$  and  $H_{A2}$ , are defined as  $K_1/\mu_0 M_s$  and  $K_2/\mu_0 M_s$ , respectively. In this model, the crystal axes  $a$ ,  $b$ , and  $c$  are aligned with the coordinate axes  $x$ ,  $y$ , and  $z$ , respectively. The unit vectors of this coordinate system are denoted by  $\hat{x}$ ,  $\hat{y}$ , and  $\hat{z}$ .

The magnon-magnon coupling can be described as an 2x2 eigenvalue problem as follows:



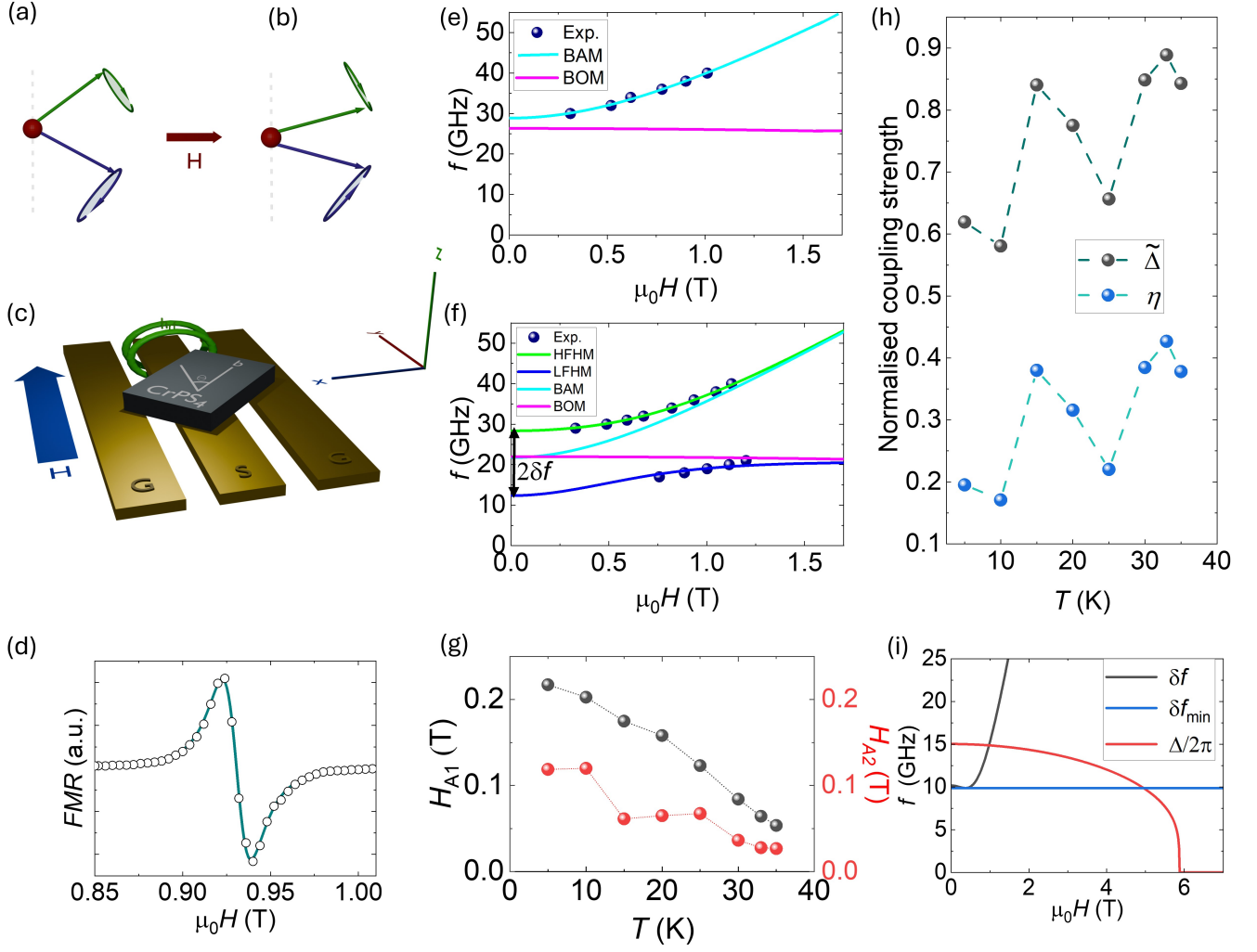


**Figure 2: Spin dynamics in CrPS<sub>4</sub> under an in-plane magnetic field.** (a-b) Schematic illustration of the magnetic moments' precession in the acoustic mode (in-phase precession) (a) and the optical mode (out-of-phase precession) (b). (c) Schematic of the configuration between coplanar waveguide (CPW), CrPS<sub>4</sub> crystal, and external in-plane magnetic field ( $H$ ). (d) Typical ferromagnetic resonance (FMR) spectra (open circles) obtained at 15 K and 15 GHz and their derived Lorentzian fitting (green line) by using Eq. S1 (see SI). (e-f) Frequency ( $f$ ) dependent FMR results obtained at 15 K, with the magnetic field applied ( $\mu_0 H$ ) along the  $a$ -axis (e) and at  $\theta = 45^\circ$  (f). The dots represent experimental data, and the fitting using Eq. 4. The fitted resonance modes are denoted as BAM, BOM, HFHM, and LFHM, representing the bare acoustic mode, bare optical mode, high-frequency hybrid mode, and low-frequency hybrid mode, respectively. (g)  $H_{A1}$  and  $H_{A2}$ , as functions of temperature. (h) Normalised magnon-magnon coupling strength,  $\tilde{\Delta}$  and  $\eta$ , as functions of temperature at  $\theta = 45^\circ$ . (i) Field dependence of  $\Delta/2\pi$  compared to the  $\delta f(H)$  at 15K, where  $\delta f_{\min}$  is the half of the minimum gap size.

$$\begin{vmatrix} \omega_{\text{BAM}}^2(H, \theta) - \omega^2 & \Delta^2(H, \theta) \\ \Delta^2(H, \theta) & \omega_{\text{BOM}}^2(H, \theta) - \omega^2 \end{vmatrix} = 0 \quad (3)$$

where  $\Delta$  denotes the magnon-magnon coupling term and  $\omega_{\text{BAM}}$  and  $\omega_{\text{BOM}}$  are the bare acoustic and

optical mode frequencies respectively. These precession modes are depicted in Fig. 2(a) and 2(b) respectively.

Solutions to this reveal that when  $\theta \neq 0^\circ, 90^\circ$  an anticrossing gap opens up at the intersection between the two modes through mode hybridisation.

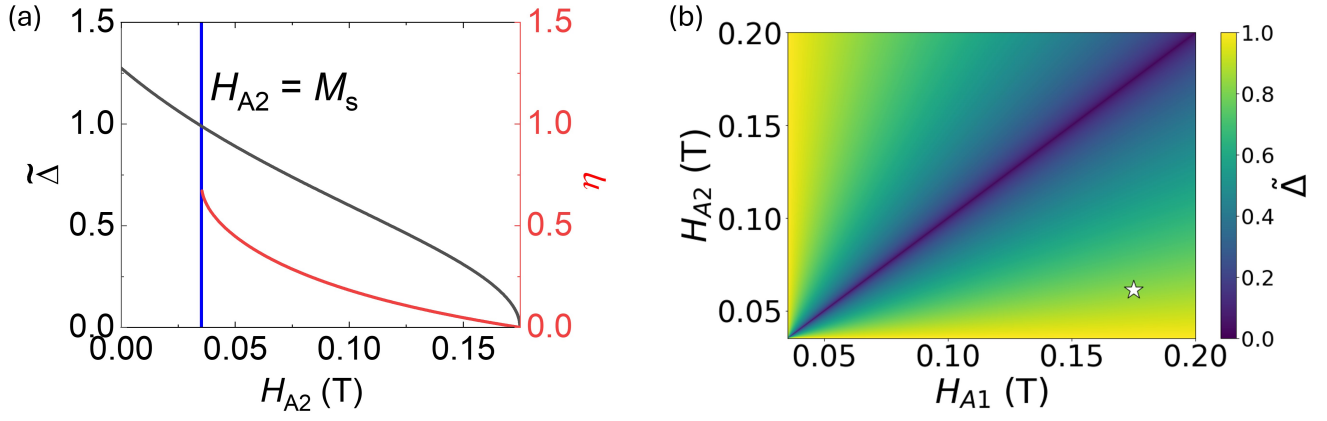


Figure 3: **Tunable normalised coupling strength via magnetic anisotropy.** (a) Simulated  $\eta$  and  $\tilde{\Delta}$  as a function of  $H_{A2}$  (b) 2D plot of  $\tilde{\Delta}$  for a fixed value of  $M_s$  at 15 K as a function of  $H_{A2}$  and  $H_{A1}$ . The star indicates the  $\tilde{\Delta}$  observed experimentally at 15 K.

The anti-crossing gap is the signature of such hybridisation and the size of the gap of the gap between the hybridised modes is defined here as  $2\delta f$  which we take at zero field as this is the point where the uncoupled modes would intersect at  $\theta = 45^\circ$ . Eq. 3 can then be used to fit experimental data as described in the following section. Solving for the real part of the above equation for  $\theta = 0^\circ$ , we obtain the eigenfrequency of the bare acoustic and optical modes, BAM and BOM respectively, given by:

$$\begin{aligned}\omega_{\text{BOM}} &= \mu_0\gamma\sqrt{(-M_s + H_{A2})\left(2H_E - M_s + H_{A1} - \frac{H^2}{2H_E - M_s + H_{A1}}\right)} \\ \omega_{\text{BAM}} &= \mu_0\gamma\sqrt{(2H_E - M_s + H_{A1})\left[\frac{H^2(2H_E + M_s - H_{A1})}{(2H_E - M_s + H_{A1})^2} - M_s + H_{A1}\right]}\end{aligned}\quad (4)$$

In Fig. 2(e), when  $\theta = 90^\circ$ , we observe that only one mode can be measured, which corresponds well with the BAM described in Eq. 4. No BOM is detected because, within this field window, the mode's frequency remains almost constant and thus cannot be detected by the field sweep measurements conducted. This observation confirms the absence of a symmetry-breaking condition in this orientation.

In Fig. 2(f), we plot the spectra obtained at 15 K in the in-plane orientation with  $\theta \approx 45^\circ$ . Here, we clearly observe magnon-magnon coupling, as evidenced by the opening of the anticrossing gap, which is comparable to the bare magnon frequencies and hence in the ultrastrong coupling regime. These two hybridised modes can be well-fitted with

the computation of Eq. 3. By fitting the coupled modes, we can extract the magnetic parameters,  $H_{A1}$ , and  $H_{A2}$ . Furthermore, we calculate the coupling strength as half the gap size,  $\delta f$ , of the coupled modes at the field at which the two uncoupled modes would intersect ( $0$  T when  $\theta = 45^\circ$ ).

The values obtained for the two in-plane anisotropy fields  $H_{A1}$  and  $H_{A2}$ , are presented in Fig. 2(g). Throughout all temperatures, the value of  $H_{A1}$  remains larger than  $H_{A2}$ . Both anisotropy fields follow a similar decreasing function of temperature, with a deviation observed in  $H_{A2}$  at 15 K and 20 K. It is typical to use the normalised coupling strength,  $\eta$ , by comparing the anticrossing gap size to the uncoupled excitation frequency.  $\eta$  is given by the following:

$$\eta = \frac{\delta f}{f_r} \quad (5)$$

where  $f_r$  represents the bare excitation frequency at the crossing.

We now define the intrinsic normalised coupling strength as follows from coupling strength defined in Eq. 3:

$$\tilde{\Delta} = \frac{\Delta}{2\pi f_r} \quad (6)$$

We then compare the normalised magnon-magnon coupling strengths as a function of temperature obtained through the two methods,  $\eta$  and  $\tilde{\Delta}$ ,

as shown in Fig. 2(h). We observe a significant difference between the two methods for all temperatures, with  $\tilde{\Delta}$  more than twice the value of  $\eta$ .

In Fig. 2(i), we plot the field dependence of  $\Delta/2\pi$  compared to the half the gaps size as a function of field ( $\delta f(H)$ ) at 15K. We demonstrate a notable difference between the two parameters at the intersection field (0 T when  $\theta = 45^\circ$ ). Additionally, we observe that  $\Delta/2\pi$  is field-dependent, as it is determined by the canting angle between the sublattice moments.  $\Delta/2\pi$  reaches a maximum when the moments are antiparallel at zero field and become zero when the angle exceeds  $45^\circ$ . This contrast with the field-independent  $\Delta/2\pi$  introduced for the SyAF, where the intrinsic symmetry breaking arises from differing  $M_s$  values between the layers [30].

To investigate further, we compare the simulated normalised coupling strength obtained from both methods as a function of  $H_{A2}$  (Fig.3(a)). Here,  $\eta$  is shown to increase as  $H_{A2}$  is decreased, reaching a

value of 0.7. At this value,  $H_{A2}$  becomes less than  $M_s$ , and the lower mode is coupled strongly enough to be completely suppressed to 0 GHz, at lower values of  $H_{A2}$  the gap size can no longer be physical.  $\tilde{\Delta}$  increases smoothly, reaching a maximum value of 1.4 when  $H_{A2}$  approaches 0 T. Notably, when the lower mode is pushed to 0 GHz, no such discontinuity is observed in  $\tilde{\Delta}$ . In fact, this corresponds to a value of exactly 1, which can be defined as the critical coupling strength, similar to the deep-strong regime in magnon-photon systems [18, 44]. The critical coupling is defined as the point when the lower hybridised mode is suppressed to 0 GHz at 0 T. Beyond this coupling strength, the lower mode is suppressed to a finite field, where stronger coupling results in a stronger suppressing field.

We now derive the analytical solution for  $\tilde{\Delta}$  from the Eq. 3 and Eq. S8 in the SI, yielding the following expression:

$$\tilde{\Delta} = \frac{\sqrt{(H_{A1} - H_{A2})H_E}}{\sqrt{H_{A2}(H_E - M_s) + H_{A1}(H_{A2} + H_E - M_s) + M_s(-2H_E + M_s)}} \quad (7)$$

Eq. 7, provides insight into how to precisely tune the coupling strength through control of the two anisotropy values. In Fig. 3(b), we present a 2D plot of the  $\tilde{\Delta}$  for a fixed value of  $M_s$  and  $H_E$  at 15 K. This demonstrates the possibility to tune the coupling strength from uncoupled to critically coupled regime through manipulation of the two anisotropy terms. Avenues for achieving this precise tuning include ionic gating, intercalation, or strain, all which has been shown to have dramatic effects on anisotropy and magnetisation in vdW magnetic materials [45, 46, 47, 48, 49].

## Spin Hall magnetoresistance in a vdW AFM

Finally, we present SMR measurements conducted on an exfoliated CrPS<sub>4</sub>(18 nm) flake on a Pt (3 nm) Hall bar device. The flake is encapsulated with a top layer of h-BN(9.5 nm) to protect it from oxi-

dation effects (Fig. 4(c)). SMR arises in bilayer systems composed of a spin source (Pt) and a magnetic layer (CrPS<sub>4</sub>) (Fig. 4(a-b)). When a current is passed through the spin source layer in the  $x$  direction, a spin current is generated in the  $z$  direction with a spin polarization in the  $y$  direction. This results in spin accumulation at the interface with the magnetic layer. A transfer of angular momentum will occur with the net magnetic moment if the polarization is non-collinear with the magnetisation, leading to an absorption of the spin current and hence an increase in the total resistance, and vice versa [50, 51]. Thus, by rotating the net moment with an external magnetic field, we observe a longitudinal resistance proportional to  $\cos^2(\alpha)$ . The change in resistance  $\Delta R_{xx}$  is given by the following equations:

$$R_{xx} = R_{xx0} - \Delta R_{xx} m_y^2 \quad (8)$$

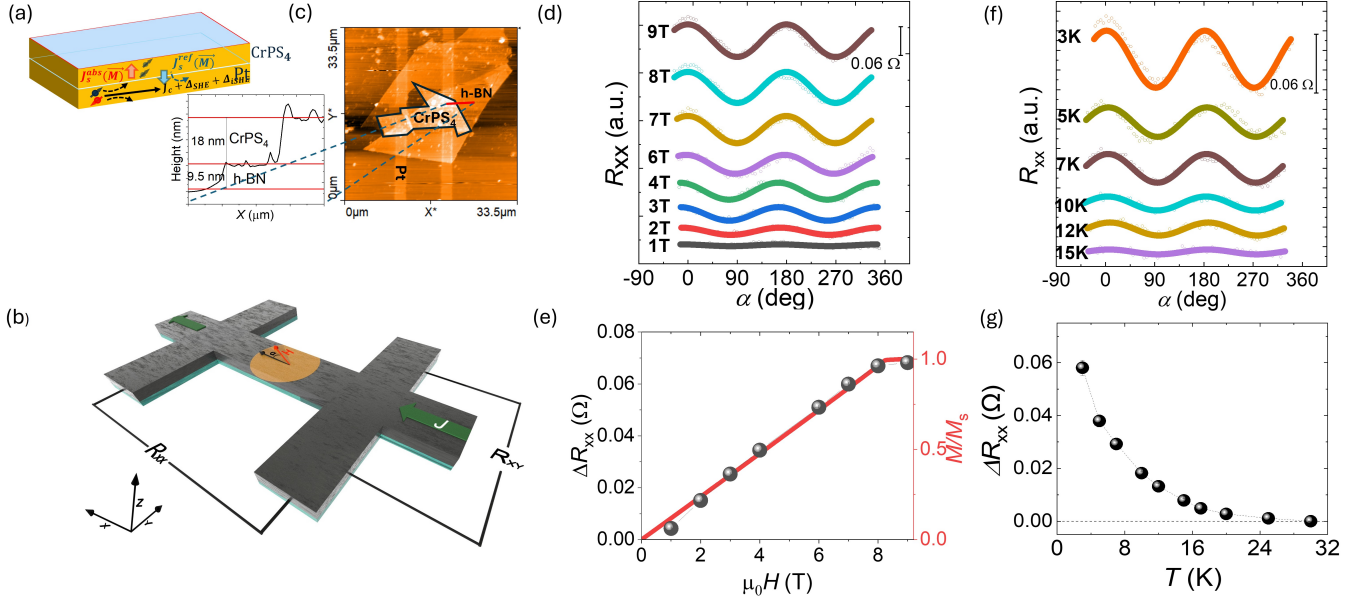


**Figure 4: Spin Hall magnetoresistance in CrPS<sub>4</sub>** (a) Schematic illustration of SMR in a bilayer device,  $J_c$  is the applied charge current,  $\Delta_{SHE}$  and  $\Delta_{iSHE}$  is the change in resistance due to the spin Hall effect (SHE) and inverse spin Hall effect (ISHE),  $J_s^{abs}$  and  $J_s^{ref}$  are the absorbed and reflected spin currents respectively. (b) Schematic illustration of the in-plane rotational measurements. The angle  $\alpha$  is defined as the angle between the magnetic field (and therefore magnetisation) and the  $x$  axis. (c) Atomic force microscopy (AFM) image of the Hall bar device. The inset shows a line scan (red bar) giving the thickness of the full stack Pt(3 nm)/CrPS<sub>4</sub>(18 nm)/h – BN(9.5 nm). (d)  $R_{xx}$  signal observed when rotating the sample in-plane under a range of applied fields up to 9 T at 3 K. (e)  $\Delta R_{xx}$  (black dots) as a function of applied magnetic field plotted against  $M/M_s$  (red). (f-g)  $\Delta R_{xx}$  as a function of temperature. The applied magnetic field is 9 T.

where  $m_y$  is the component of the magnetisation along the  $y$  axis. We measure the longitudinal resistance ( $R_{xx}$ ) and transverse resistance ( $R_{xy}$ ) as a function of the angle of the field with respect to the applied current using the 4-point probe method. By comparing the data with a reference sample (Pt), we can confirm whether the measured signal originates from the generated spin current. When comparing the values of the angular-dependent magnetoresistance (ADMR) for out-of-plane rotations (see Fig. S5(a-c), SI), we observe a large magnetoresistance effect in both samples. We attribute this to a significant weak anti-localization (WAL) signal that occurs in Pt at low temperatures and high fields as observed previously by Oyanagi et al.[52] and depicted in more detail in the SI (See Fig. S7). This effect makes it difficult to quantify the SMR signal in this orientation. Instead, we focus on the in-plane orientation and rotate through the angle  $\alpha$ . In this

orientation, it has been shown that we would not expect any signal from WAL [52]. Hanle magnetoresistance could also introduce an SMR-like angular dependence [53]; however, we can eliminate this possibility by comparison with a reference sample of Pt/SiO<sub>2</sub>. We can confirm in this orientation there is no significant SMR-like signal, and hence we can exclude Hanle magnetoresistance in these devices (see Fig. S7(d), SI).

By measuring the  $R_{xx}$  for  $\alpha$  rotation at a range of fields (Fig. 4(d)) and temperatures (Fig. 4(f)), we are able to extract the amplitude of the SMR. In Fig. 4(e), the  $\Delta R_{xx}$  amplitude is observed to increase linearly at first then saturating at around 8 T, by plotting against the VSM data, we can see that this agrees well with the magnetic moment, indicating that the SMR field dependence in this range is dominated by the magnetic moment as expected. The SMR amplitude observed is the same order of



magnitude seen in other vdW and thin film AFM devices [37, 54]. In Fig. 4(g), we plot the temperature dependence of the  $\Delta R_{xx}$ . We observe a monotonic decrease within the temperature range, approaching zero as we approach  $T_N$ . Due to the relative thickness of the exfoliated flake, we assume that the  $T_N$  in this flake is close to that of the bulk, as we are not within the few-layer regime where the transition temperature will start to drop significantly [55]. The observed temperature dependence is related to the decreasing magnetic moment of the sample as a function of temperature, indicating that this is the dominating factor controlling the SMR amplitude, this is similar to the behaviour observed in other vdW AFM [35]. In addition to this, we observe the presence of a SMR like signal fitting to  $\cos(\alpha)\sin(\alpha)$  in  $R_{xy}$  (see Fig. S6, SI). This further confirms that Hanle magnetoresistance is not the origin of the SMR signal observed in Fig. 4(d-g). This demonstrates the possibility to read-out the magnetic state of exfoliated flakes through spin current. Furthermore, it allows for future studies using spin-orbit torque (SOT) to switch or manipulate spin textures and magnetisation in exfoliated vdW devices [56].

In conclusion, our investigation has revealed the temperature-dependence of the ultrastrong magnon-magnon coupling in the vdW AFM CrPS<sub>4</sub>. This coupling is attributed to the interplay of in-plane orthorhombic anisotropy, saturation magnetisation, and the exchange field. We evaluated the normalised coupling strength using two approaches: the gap size  $\eta$  and the intrinsic coupling strength  $\tilde{\Delta}$ . Our findings indicate that, in systems with intrinsic symmetry-breaking anisotropy, these two methods yield notably different normalised coupling strength values. We further provide an analytical description of  $\tilde{\Delta}$ , showing how tuning anisotropy values beyond a critical point could enhance coupling, similar to the deep-strong coupling regime in magnon-photon systems. Additionally, we demonstrate SMR in an exfoliated Pt/CrPS<sub>4</sub> device. Here, we show the feasibility of electrically detecting the magnetic state in such devices, thereby providing a pathway for the electrical readout of semiconducting vdW AFMs. This advancement not only enhances our understanding of the spin dynamics and magneto-transport of

vdW AFMs, but also opens avenues for their utilization in next-generation spintronic and magnonic devices.

## References

- [1] Jungwirth, T., Marti, X., Wadley, P. & Wunderlich, J. Antiferromagnetic spintronics. *Nat. Nano.* **11**, 231–241 (2016).
- [2] Baltz, V. *et al.* Antiferromagnetic spintronics. *Rev. of Mod. Phys.* **90**, 015005 (2018).
- [3] Gomonay, O., Baltz, V., Brataas, A. & Tserkovnyak, Y. Antiferromagnetic spin textures and dynamics. *Nat. Phys.* **14**, 213–216 (2018).
- [4] Novoselov, K. S. *et al.* Electric field effect in atomically thin carbon films. *Science* **306**, 666–669 (2004).
- [5] Mermin, N. D. & Wagner, H. Absence of ferromagnetism or antiferromagnetism in one-or two-dimensional isotropic heisenberg models. *Phys. Rev. Lett.* **17**, 1133 (1966).
- [6] Gong, C. *et al.* Discovery of intrinsic ferromagnetism in two-dimensional van der Waals crystals. *Nature* **546**, 265–269 (2017).
- [7] Huang, B. *et al.* Layer-dependent ferromagnetism in a van der Waals crystal down to the monolayer limit. *Nature* **546**, 270–273 (2017).
- [8] Duine, R., Lee, K.-J., Parkin, S. S. & Stiles, M. D. Synthetic antiferromagnetic spintronics. *Nat. Phys.* **14**, 217–219 (2018).
- [9] MacNeill, D. *et al.* Gigahertz frequency antiferromagnetic resonance and strong magnon-magnon coupling in the layered crystal CrCl<sub>3</sub>. *Phys. Rev. Lett.* **123**, 047204 (2019).
- [10] Peng, Y. *et al.* Magnetic structure and metamagnetic transitions in the van der Waals antiferromagnet CrPS<sub>4</sub>. *Adv. Mat.* **32**, 2001200 (2020).

- [11] Awschalom, D. D. *et al.* Quantum engineering with hybrid magnonic systems and materials. *IEEE Transactions on Quantum Engineering* **2**, 1–36 (2021).
- [12] Lachance-Quirion, D., Tabuchi, Y., Gloppe, A., Usami, K. & Nakamura, Y. Hybrid quantum systems based on magnonics. *Appl. Phys. Express* **12**, 070101 (2019).
- [13] Tabuchi, Y. *et al.* Coherent coupling between a ferromagnetic magnon and a superconducting qubit. *Science* **349**, 405–408 (2015).
- [14] Lachance-Quirion, D. *et al.* Entanglement-based single-shot detection of a single magnon with a superconducting qubit. *Science* **367**, 425–428 (2020).
- [15] Zollitsch, C. W. *et al.* Probing spin dynamics of ultra-thin van der waals magnets via photon-magnon coupling. *Nat. Comms.* **14**, 2619 (2023).
- [16] Niemczyk, T. *et al.* Circuit quantum electrodynamics in the ultrastrong-coupling regime. *Nat. Phys.* **6**, 772–776 (2010).
- [17] Forn-Díaz, P., Lamata, L., Rico, E., Kono, J. & Solano, E. Ultrastrong coupling regimes of light-matter interaction. *Rev. of Mod. Phys.* **91**, 025005 (2019).
- [18] Frisk Kockum, A., Miranowicz, A. & De Liberato, S. Ultrastrong coupling between light and matter. *Nat. Rev. Phys.* **1** (2019).
- [19] Forn-Díaz, P., Lamata, L., Rico, E., Kono, J. & Solano, E. Ultrastrong coupling regimes of light-matter interaction. *Rev. Mod. Phys.* **91**, 025005 (2019).
- [20] Hopfield, J. Theory of the contribution of excitons to the complex dielectric constant of crystals. *Phys. Rev.* **112**, 1555 (1958).
- [21] Wang, Y. *et al.* Ultrastrong to nearly deep-strong magnon-magnon coupling with a high degree of freedom in synthetic antiferromagnets. *Nat. Comms.* **15**, 2077 (2024).
- [22] Frisk Kockum, A., Miranowicz, A., De Liberato, S., Savasta, S. & Nori, F. Ultrastrong coupling between light and matter. *Nat. Rev. Phys.* **1**, 19–40 (2019).
- [23] Wang, Y. K. & Hioe, F. Phase transition in the dicke model of superradiance. *Phys. Rev. A* **7**, 831 (1973).
- [24] Sud, A., Yamamoto, K., Suzuki, K., Mizukami, S. & Kurebayashi, H. Magnon-magnon coupling in synthetic ferrimagnets. *Phys. Rev. B* **108**, 104407 (2023).
- [25] Chen, J. *et al.* Strong interlayer magnon-magnon coupling in magnetic metal-insulator hybrid nanostructures. *Phys. Rev. Lett.* **120**, 217202 (2018).
- [26] Dion, T. *et al.* Ultrastrong magnon-magnon coupling and chiral spin-texture control in a dipolar 3d multilayered artificial spin-vortex ice. *Nature Communications* **15**, 4077 (2024).
- [27] Liensberger, L. *et al.* Exchange-enhanced ultrastrong magnon-magnon coupling in a compensated ferrimagnet. *Phys. Rev. Lett.* **123**, 117204 (2019).
- [28] Makiyara, T. *et al.* Ultrastrong magnon-magnon coupling dominated by antiresonant interactions. *Nat. Comm.* **12**, 3115 (2021).
- [29] Li, W. *et al.* Ultrastrong magnon-magnon coupling and chirality switching in antiferromagnet CrPS<sub>4</sub>. *Adv. Funct. Mater.* **33**, 2303781 (2023).
- [30] Li, M., Lu, J. & He, W. Symmetry breaking induced magnon-magnon coupling in synthetic antiferromagnets. *Physical Review B* **103**, 064429 (2021).
- [31] Sinova, J., Valenzuela, S. O., Wunderlich, J., Back, C. & Jungwirth, T. Spin hall effects. *Rev. of Mod. Phys.* **87**, 1213 (2015).
- [32] Cubukcu, M. *et al.* Spin-orbit torque magnetization switching of a three-terminal perpendicular magnetic tunnel junction. *Appl. Phys. Lett.* **104** (2014).

- [33] Cubukcu, M. *et al.* Ultra-fast perpendicular spin-orbit torque mram. *IEEE Transactions on Magnetics* **54**, 1–4 (2018).
- [34] Chen, Y.-T. *et al.* Theory of spin hall magnetoresistance. *Phys. Rev. B.* **87**, 144411 (2013).
- [35] Feringa, F., Bauer, G. & Van Wees, B. Observation of magnetization surface textures of the van der waals antiferromagnet FePS<sub>3</sub> by spin hall magnetoresistance. *Phys. Rev. B.* **105**, 214408 (2022).
- [36] Sugi, K. *et al.* Spin hall magnetoresistive detection of easy-plane magnetic order in the van der waals antiferromagnet NiPS<sub>3</sub>. *Phys. Rev. B.* **108**, 064434 (2023).
- [37] Wu, R. *et al.* Magnetotransport study of van der waals CrPS<sub>4</sub>/(Pt, Pd) heterostructures: Spin-flop transition and room-temperature anomalous hall effect. *Phys. Rev. Appl.* **17**, 064038 (2022).
- [38] Tang, C. *et al.* Spin dynamics in van der waals magnetic systems. *Physics Reports* **1032**, 1–36 (2023).
- [39] Lee, J. *et al.* Structural and optical properties of single-and few-layer magnetic semiconductor CrPS<sub>4</sub>. *ACS Nano* **11**, 10935–10944 (2017).
- [40] Louisy, A., Ouvrard, G., Schleich, D. & Brec, R. Physical properties and lithium intercalates of CrPS<sub>4</sub>. *Solid State Comms.* **28**, 61–66 (1978).
- [41] Diehl, R. & Carpentier, C.-D. The crystal structure of chromium thiophosphate, CrPS<sub>4</sub>. *A. Cryst. Sec. B: Struct. Cryst. and Cryst. Chem.* **33**, 1399–1404 (1977).
- [42] Joe, M., Lee, J. & Lee, C. Dominant in-plane cleavage direction of CrPS<sub>4</sub>. *Comp. Mat. Sci.* **162**, 277–280 (2019).
- [43] Keffer, F. & Kittel, C. Theory of antiferromagnetic resonance. *Phys. Rev.* **85**, 329 (1952).
- [44] Casanova, J., Romero, G., Lizuain, I., García-Ripoll, J. J. & Solano, E. Deep strong coupling regime of the jaynes-cummings model. *Physical review letters* **105**, 263603 (2010).
- [45] Verzhbitskiy, I. A. *et al.* Controlling the magnetic anisotropy in Cr<sub>2</sub>Ge<sub>2</sub>Te<sub>6</sub> by electrostatic gating. *Nat. Elec.* **3**, 460–465 (2020).
- [46] Khan, S. *et al.* Spin-glass states generated in a van der waals magnet by alkali-ion intercalation. *Advanced Materials* **36**, 2400270 (2024).
- [47] Tang, C., Zhang, L. & Du, A. Tunable magnetic anisotropy in 2d magnets via molecular adsorption. *J. of Mat. Chem. C* **8**, 14948–14953 (2020).
- [48] Webster, L. & Yan, J.-A. Strain-tunable magnetic anisotropy in monolayer CrCl<sub>3</sub>, CrBr<sub>3</sub>, and CrI<sub>3</sub>. *Phys. Rev. B.* **98**, 144411 (2018).
- [49] Qi, S. *et al.* Giant electrically tunable magnon transport anisotropy in a van der Waals antiferromagnetic insulator. *Nat. Comms.* **14**, 2526 (2023).
- [50] Huang, S.-Y. *et al.* Transport magnetic proximity effects in platinum. *Phys. Rev. Lett.* **109**, 107204 (2012).
- [51] Nakayama, H. *et al.* Spin hall magnetoresistance induced by a nonequilibrium proximity effect. *Phys Rev. Lett.* **110**, 206601 (2013).
- [52] Oyanagi, K. *et al.* Paramagnetic spin hall magnetoresistance. *Phys. Rev. B* **104**, 134428 (2021).
- [53] Vélez, S. *et al.* Hanle magnetoresistance in thin metal films with strong spin-orbit coupling. *Phys Rev. Lett.* **116**, 016603 (2016).
- [54] Baldrati, L. *et al.* Full angular dependence of the spin hall and ordinary magnetoresistance in epitaxial antiferromagnetic NiO (001)/Pt thin films. *Phys. Rev. B.* **98**, 024422 (2018).
- [55] Son, J. *et al.* Air-stable and layer-dependent ferromagnetism in atomically thin van der

waals CrPS<sub>4</sub>. *ACS nano* **15**, 16904–16912 (2021).

- [56] Kurebayashi, H., Garcia, J. H., Khan, S., Sinova, J. & Roche, S. Magnetism, symmetry and spin transport in van der waals layered systems. *Nature Reviews Physics* **4**, 150–166 (2022).
- [57] Budniak, A. K. *et al.* Exfoliated CrPS<sub>4</sub> with promising photoconductivity. *Small* **16**, 1905924 (2020).

## Methods

### Material growth

Chromium thiophosphate (CrPS<sub>4</sub>) was synthesized in a quartz ampoule via physical vapor transport (PVT) – without any transporting agent [57]. About half of a gram of stoichiometric elements mixture (metal chromium powder, red phosphorus powder, and elemental sulfur powder (all purchased from Sigma-Aldrich), Cr:P:S = 1:1:4) was ground in agate mortar, moved into quartz ampoule, evacuated to high vacuum (below  $5 \times 10^{-6}$  mBar) by turbomolecular pump and closed by a flamer. The sealed ampoule was put into a two-zone furnace, that was calibrated in a way that the mixture of elements was kept at 750 °C and the deposition zone was 710 °C. The ampoule was warmed from room temperature to designated ones within five hours, after four days the furnace was turned off and the sample was allowed to cool down naturally. Then the ampoule was opened, and only recrystallized, large, pure CrPS<sub>4</sub> crystals from the deposition zone (710 °C) were collected.

### Device fabrication

The pre-patterned Pt Hall bar device was fabricated using a Heidelberg direct writing system and Pt was deposited by electron beam evaporation technique followed by a lift-off process. The Si/SiO<sub>2</sub> substrate was first cleaned using acetone and IPA. Then spin resist with LOR and S1805, baking them ten and one minutes at 190 °C and 115 °C, respectively. Then the Hall bar pattern was written by

Heidelberg direct writing system followed by a developing process with MF319 developer, where the width of the Hall bar arms and current line are 2  $\mu$ m and 3  $\mu$ m, respectively. The Pt (3 nm) was deposited using an electron beam evaporation system under a pressure of  $3 \times 10^{-6}$  mbar. Finally, the lift-off process was carried out using DMSO and the device was dried with nitrogen flow. CrPS<sub>4</sub> flakes were exfoliated from bulk using blue Nitto tape, in the typical scotch tape method. The tape is brought into contact with SiO<sub>2</sub> (280 nm)/Si wafers heated to 80 °C, that have been cleaned with acetone and IPA and then plasma cleaned in a Moorfields RIE chamber for 5mins at 5W with Argon flow at 15 sccm housed within the inert environment. A HQ graphene transfer system is used to identify suitable flakes and carry out the transfer with 40 % PPC mounted on a PDMS stamp.

### Measurement technique

To investigate the magnetism, spin dynamics and transport in the vdW AFM CrPS<sub>4</sub>, we performed magnetometry, ferromagnetic resonance (FMR) and magneto-transport measurements using a Quantum Design Physical Property Measurement System (PPMS). The PPMS is equipped with a vibrating sample magnetometer (VSM), a NanOsc CryoFMR probe for coplanar waveguide (CPW)-FMR spectroscopy covering the frequency range of 2 - 40 GHz, and an electrical transport setup. This PPMS configuration enables the application of magnetic fields up to 9 T and provides precise temperature control down to 1.8 K.

The devices are wire-bonded to the PPMS puck and held by GE varnish. For the electrical measurements an alternative current (AC) current of 30  $\mu$ A was applied.

### Data availability

All relevant data are available from the corresponding authors upon reasonable request.

### Acknowledgements

C.W.F.F. and M.C. acknowledge support from the UK National Quantum Technologies pro-



gramme. C.W.F.F. and H.Y. thank EPSRC for support through EPSRC DTP Case studentship (EP/T517793/1). H.K. acknowledges support from EPSRC via EP/T006749/1 and EP/V035630/1. A.K.B., M.B. and G.E. acknowledges support from the Ministry of Education (MOE), Singapore, under AcRF Tier 3 (MOE2018-T3-1-005). We thank O. Lee for developing Fig. 4(b) and assistance with Blender.

## **Author contributions**

C.W.W.F., H.K., and M.C. conceived and planned the project. C.W.W.F. and M.C. conducted VSM, FMR, and magneto-transport measurements, as well as data analysis. C.W.W.F. conducted AFM measurements. H.Y. and C.W.W.F. carried out MuMax<sup>3</sup> simulations in the SI. A.K.B. grew the CrPS<sub>4</sub> crystal under the supervision of G.E. and performed XRD measurements under supervision of M.B. Z.X., H.D.L. and T.T. grew platinum films. Z.X. fabricated platinum Hall bars. C.W.F.F. performed transfer of flakes onto devices. C.W.W.F. and M.C. wrote the paper. All authors contributed to discussions on the results and provided feedback on the manuscript.

## **Competing interests**

The authors declare no competing interests.

## **Additional information**

**Supplementary information.** The online version contains supplementary material available at (link).

**Correspondence** and requests for materials should be addressed to C. W. F. Freeman or M. Cubukcu.